COO-3158-78

THE STUDY OF DEFECTS AND RADIATION DAMAGE IN SOLIDS BY FIELD-ION AND ATOM-PROBE MICROSCOPY

by

David N. Seidman

Cornell University

Ithaca, New York 14853

June 1979

Report #4106

Prepared for

THE U.S. DEPARTMENT OF ENERGY UNDER

CONTRACT NO. EY-76-S-02-3158.*000.

DISCLAIMER

THE STUDY OF DEFECTS AND RADIATION DAMAGE IN SOLIDS BY FIELD-ION AND ATOM-PROBE MICROSCOPY

by

David N. Seidman

Cornell University, Department of Materials Science and Engineering
and the Materials Science Center,
Bard Hall, Ithaca, New York 14853

ABSTRACT

A brief review is presented of: (1) the basic physical principles of the field-ion and atom-probe microscopes; (2) the many applications of these instruments to the study of defects and radiation damage in solids; and (3) the application of the atom-probe field-ion microscope to the study of the behavior of implanted ^{3}He and ^{4}He in tungsten. The paper is heavily referenced so that the reader can pursue his specific research interests in detail.

1. INTRODUCTION

In this short paper an attempt is made to introduce the reader to the basic physical ideas involved in the field-ion and atom-probe field-ion microscope techniques (§2), and to the applications of these techniques to the study of defects and radiation damage in solids (§3). The final section (§4) discusses, in précis form, the application of the atom-probe field-ion microscope to the study of the behavior of implanted ^{3}He and ^{4}He atoms in tungsten. The paper is heavily referenced so that the reader can pursue his specific research interests in detail.

2. GENERAL BACKGROUND MATERIAL

The invention of the field-ion microscope (FIM) and the atom-probe FIM by Müller[1,2] has provided the experimentalist with tools which allow both the direct observation of all the common defects (point, line and planar) on an atomic scale and the simultaneous determination of chemical effects on an atomic scale (the minimum detectable mass is the mass of a single atom).

The atomic structure of the direct lattice is observed for those atoms which lie on the surface of a sharply pointed ($\sim$200 to 500Å in diameter) FIM specimen; the area imaged is $\sim 10^{-10}$ to 10^{-11} cm^2. The information concerning the positions of the atoms is carried to a phosphor screen or a channel electron multiplier array[3,4] by an imaging gas which is typically helium or neon. The imaging gas atoms are ionized, by a tunneling mechanism, in the high local electric fields ($\sim$4.5 V Å^{-1} to ionize a helium atom) that exist at the site of individual atoms as a result of a positive potential applied to a sharply pointed FIM specimen.[5] The positively-charged ions are repelled from the specimen and then travel along the electric field lines to the phosphor screen which is at earth potential; typically the phosphor screen is at a distance of between 4 to 10 cm from the FIM specimen. The image formed of the atoms on the surface of

the FIM specimen, in the above manner, constitutes a point projection image with sufficient magnification to resolve individual atoms.

The interior of the specimen can be examined employing the field-evaporation process. The latter process consists of increasing the electric field to a value such that the potential energy curve of an ion on the surface of the specimen (this statement assumes that the state in which the metal atoms exist on the surface of the specimen is the ionic state) is deformed by the applied field to form a Schottky hump.[6] The ions then evaporate (sublime) by either jumping over this small Schottky hump or by tunneling through it; this process is called field desorbtion or field evaporation. The field evaporation process can be controlled by applying the positive potential in the form of short (1 to 10 msec in width) high-voltage pulses. This latter technique is called pulse field evaporation; it is possible by this technique to dissect an atomic plane one or two atoms at a time. Thus, the atoms contained within the interior of the specimen can be imaged, albeit at the surface, at a rate which is determined by the experimentalist. In practice one can examine $\approx 10^{-16}$ to 10^{-17} cm^3 of material, during the course of one experiment, via the pulse field evaporation technique. At Cornell we have developed semi-automated techniques for the process of applying the field evaporation pulse in conjunction with the simultaneous recording of large numbers of frames of 35 mm ciné film [$(15 \text{ to } 30)\times 10^3$ frames per day] as well as developing techniques for the scanning of this film.[7] It is clear, with the advantage of hindsight, that these two steps were essential to the successful application of the FIM technique to problems in the field of radiation damage.

The invention[2] of the time-of-flight (TOF) atom-probe FIM has provided us with a unique instrument for the study of the interaction of impurity atoms or alloying elements with point, line or planar defects. The TOF atom-probe FIM (hereafter called an atom probe) consists of an FIM combined with a special TOF mass spectrometer. This spectrometer allows the investigator to identify chemically any atom that appears in an FIM image. Thus, it is now possible to

II. Volume Change of Migration (Δv_{1i}^{m}) of SIAs

a. Measured Δv_{1i}^{m} for the SIA in W, Pt and Mo in detail. Experiments were also performed on Ni_4Mo and Pt_3Co but in less detail.

b. For further details see reference numbers 18, 19, 27, 28, 31, 37, 38, 39, 40, 41.

III. Binding Enthalpy of an SIA to a Solute Atom (Δh^{b})

a. Measured Δh^{b} by determining a dissociation enthalpy (Δh^{d}) and then determining Δh^{b} from the expression $\Delta h^{d} = \Delta h^{b} + \Delta h_{1i}^{m}$. The system Pt(Au) was studied in great detail and two detrapping stages (II_B and II_C) were observed in Stage II.

b. The systems W(Re) and W(C) were also studied but in less detail.

c. For further details see reference numbers 19, 21, 33, 36, 39, 40.

IV. Diffusive Properties of Vacancies

a. Measured ratio of divacancy concentration to monovacancy concentration for one quench temperature in platinum specimens.

b. From (a) it was possible to determine the Gibbs free binding energy (Δg_{2v}^{b}) in platinum.

c. Measured vacancy concentration in tungsten specimens which had been quenched from near the melting point.

d. The measurements discussed in (a) to (c) are important for interpreting the high-temperature self-diffusion data by point-defect mechanisms.

e. For further details see reference numbers 18, 42, 43, 44, 45, 46.

V. Diffusive Properties of Gases in Metals

a. Diffusion of ^{3}He and ^{4}He in tungsten and platinum.

b. Diffusion of ^{1}H and ^{2}H in tungsten.

c. For further details see reference numbers 47, 48, 49, 50, 51, 52.

VI. Range Profiles of Low-Energy Implanted Gases in Metals

a. Range profiles of ^{3}He and ^{4}He in tungsten and platinum (100 to 1500 eV singly-charged ions).

b. Range profiles of ^{1}H and ^{2}H in tungsten.

c. For further details see reference numbers 47, 48, 49, 50, 51, 52.

VII. Point-Defect Structure of Depleted Zones: The Primary State of Radiation Damage

a. Depleted zones in ion-irradiated metals [W, Pt, Pt(Au)]

(i) Dimensions of depleted zones (DZs)

(ii) Number of vacancies per DZ.

(iii) Vacancy concentration within DZs

(iv) The distribution of 1st-nearest-neighbor vacancy clusters

(v) The radial distribution function (RDF) for the vacancies out to 9th-nearest-neighbor

b. Effect of projectile mass (M_1) on the structure of DZs at constant projectile energy

c. Effect of M_1 on the structure of DZs at constant reduced energy (ε)

d. For further details see reference numbers 18, 20, 21, 49, 53, 54, 55, 56, 57.

VIII. Damage Profiles

a. Ne^{+} (250 to 2500 eV) irradiated Ni_4Mo and Pt_3Co (order-disorder alloys). Damage profiles determined by measuring the change in the Bragg-Williams long-range order parameter(S) as a function of depth.

b. 30 keV W^{+}, Cr^{+} or Mo^{+} Irradiated Tungsten.

c. For further details see reference numbers 38, 49.

IX. Sputtering of Surfaces

a. The sputtering of a metal surface is the result of the intersection of a collision cascade with it. In this work we compared the vacancy structure of depleted zones, produced by 30 keV W^+, Mo^+, Cr^+, Cu^+ or Ar^+ ions, that were found to have intersected the surface of a tungsten FIM specimen with the depleted zones found in the bulk of the specimen.

b. For further details see reference number 57.

X. Voids in Neutron-Irradiated Metals [Mo, Mo(Ti), Fe(Cu)]

a. Void number density: need a number density of $\approx 10^{17} cm^{-3}$ in order to be able to make measurements.

b. Void size distribution: same comment as in X.a. applicable.

c. Direct observation of segregation.

d. For further details see reference numbers 58, 59, 60.

XI. Distribution of SIAs in the Primary Damage State

a. SIA distribution in ion-irradiated tungsten (30 keV W^+, Mo^+, Cr^+).

b. Range of replacement collision sequences. (RCSs)

c. For further details see reference numbers 53, 61.

4. RANGE PROFILES OF LOW-ENERGY (100 to 1500 eV) IMPLANTED ^3He AND ^4He ATOMS AND THE DIFFUSIVITY OF ^3He AND ^4He IN TUNGSTEN

4.1 General Background

Current interest in the fundamental properties of helium in metals has been generated by the materials problems associated with the development of the liquid-metal fast-breeder reactor[62] and the controlled thermonuclear reactor.[63] However, because of a lack of appropriate experimental techniques the investigations of the range of low-energy (<1 keV) implanted He ions and

the diffusivity of He in metals have been largely theoretical.[64-66] Measurement of the range profiles of implanted He ions have been confined to energies[67] >1 keV; furthermore, the measurement of both the range profiles of implanted He and the diffusivity of He in metals have relied exclusively on the trapping of He at lattice defects introduced as a result of heavy-ion irradiation.[68]

The accomplishments of our research on helium implanted in tungsten were: (1) the establishment of the ability of the atom-probe FIM to detect either implanted ^{3}He or ^{4}He atoms retained in a perfect (i.e., totally defect-free) lattice; (2) the detection of the presence of an isolated and immobile ^{3}He or ^{4}He atom in a perfect tungsten lattice; (3) the measurement of the range profiles of low-energy (100 to 1500 eV) implanted ^{3}He or ^{4}He atoms in a perfect tungsten lattice; and (4) the measurement of the diffusivities of ^{3}He and ^{4}He in a perfect tungsten lattice.

The basic physical ideas involved in the experimental procedures are illustrated sequentially in Fig. 1. A single-crystal W FIM specimen, at an irradiation temperature (T_i), was irradiated <u>in situ</u> with $^3He^+$ or $^4He^+$ ions parallel to the [110] direction as shown in Fig. 1(a). To study the diffusional behavior of either ^{3}He or ^{4}He in tungsten it was necessary to implant the helium under the condition of <u>no</u> radiation damage. For example, a 300-eV ^{4}He atom can transfer a maximum energy of $\sim$25 eV to a W atom in a head-on two-body elastic collision. Since the minimum displacement energy for the production of a stable Frenkel pair in W is $\gtrsim$42 eV[69], no self-interstitial atoms (SIA's) or vacancies are created at an implantation energy of 300 eV for either ^{3}He or ^{4}He. Thus for the diffusion experiments a standard implantation energy of 300 eV was employed. With no SIA's or vacancies present to act as trapping centers, implanted ^{3}He or ^{4}He atoms can remain in the specimen only if ^{3}He or ^{4}He is immobile at T_i. Thus, the state of the W specimen after an implantation consisted of immobile

interstitial ^{3}He or ^{4}He atoms implanted in a perfect W lattice with a depth distribution that was determined solely by the range profile of the low-energy ions. Next the specimen was analyzed chemically, by the atom-probe technique, at a standard reference temperature (T_r), where $T_r \leq T_i$, and a ^{3}He or ^{4}He integral profile was plotted as shown in Fig. 1(b); this was an integral profile since it measured the cumulative number of ^{3}He or ^{4}He atoms as a function of the cumulative number of W atoms (depth) from the irradiated surface. The depth scale was converted from cumulative number of W atoms to angstroms from the measured number of W atoms per (110) plane contained within the cylindrical element samples; see Fig. 1(a). Finally the ^{3}He or ^{4}He range profile, Fig. 1(c), may be constructed by taking the first derivative of the integral profile shown in Fig. 1(b); or alternatively by plotting a frequency distribution diagram.

A novel technique for the determination of an absolute depth scale was developed; Fig. 2 schematically illustrates the method. During the atom-probe analysis the specimen was oriented and the magnification adjusted so that only the central portion of the W(110) plane was chemically analyzed. The specimen was then pulse field evaporated through the repeated application of high-voltage pulses. Three successive stages in the pulse field evaporation of one (110) plane are indicated in Fig. 2(a). As the plane was pulsed, field-evaporated atoms were detected as indicated by the positive slope in Fig. 2(b). When a plane was completely evaporated the slope of the curve in Fig. 2(b) returned to zero. Therefore the removal of one (110) plane resulted in a single-step increase in the plot of the number of W atoms detected versus the number of field-evaporation pulses applied to the specimen. Since the W lattice was employed as a depth marker, the absolute depth of each implanted ^{3}He or ^{4}He atom from the initial irradiated surface was measured to within one (110) interplanar spacing ($\sim$2.24 Å)

independent of the total depth of analysis. Thus the spatial depth resolution of the atom-probe technique is limited solely by the interplanar spacing of the region being analyzed.

4.2. Integral and range profiles of low-energy implanted ^{3}He and ^{4}He atoms

In this section we present a number of integral profiles and range profiles for both ^{3}He and ^{4}He which had been implanted in tungsten at 60 K. The term integral profile reflects the manner in which the data was recorded [see fig. 1(b)], whereas the range profile was constructed by plotting a frequency distribution diagram from the integral profile [see fig. 1(c)]. The range profile can also be obtained by drawing a smooth curve throuth the integral profile and taking the first derivative of this curve. In all cases we have obtained the range profile by the former rather than the latter technique.

Figure 3 exhibits ^{3}He integral profiles for the implantation energies 100, 500 and 1500 eV; the 100 eV profile is a composite of two integral profiles each with a dose of 4.7×10^{15} ion cm^{-2}; both the 500 and 1500 eV integral profiles were obtained after implanting to a dose of 3×10^{15} ion cm^{-2}. In fig. 4 we show a composite range profile for 300 eV ^{3}He ions; this range profile was constructed from seven integral profiles and includes a total of 385 ^{3}He events; the values of the mean range ($\bar{x}$) and the straggling (Δx) are 54.9 and 41.5 Å respectively.

Figure 5 exhibits ^{4}He integral profiles for the implanation energies 150, 500 and 1000 eV; the 150 eV data consists of a single integral profile for a specimen that had been implanted to a dose of 3×10^{15} ion cm^{-2}; the 1000 eV data is for a single integral profile for a specimen that had received a dose of 4×10^{15} ion cm^{-2}. In fig. 10 we show a composite range profile for a 1000 eV ^{4}He implantation; this range profile was constructed from three integral range profiles and includes a total of 147 ^{4}He events; the values of x and Δx are 133 and 104.2 Å respectively.

All of the ^{3}He and ^{4}He integral profiles exhibited positive skewness as expected for low-energy irradiations (Biersack and Haggmark[70]); this implied that the mean range[7] was greater than the most probable range (or mode) and that the majority of the large deviations were to the right (positive) side of $\bar{x}$. The coefficient of skewness is related to the third moment about $\bar{x}$ and is given (Parratt[71]) by:

$$\text{Coefficient of Skewness} = \frac{\sum_{i=1}^{n} (x_i - \bar{x})^3}{N(\Delta x)^3}, \qquad (1)$$

where x_i is the measured depth of the i^{th} detected helium atom from the initial irradiated surface, N is the total number of helium events detected and Δx is the standard deviation or straggling.

The values of $\bar{x}$ and Δx were calculated directly from the integral profiles for the ^{3}He and ^{4}He implantations. The values $\bar{x}$ and Δx were referred to as uncorrected quantities. The reason for this is that $\bar{x}$ and Δx must be corrected for the following systematic errors: (1) the random arrival of helium atoms at the surface of the specimen, from the residual partial pressure of helium, during the atom-probe analysis of the irradiated specimen; and (2) the effect of the finite curvature of the FIM tip. A detailed analysis of the above effects is given elsewhere (Amano, Wagner and Seidman[72]), where it was shown that the corrections to $\bar{x}$ and Δx were very minimal in our experiments. Thus we shall not employ the word uncorrected any further in this paper.

Figure 7 exhibits $\bar{x}$ (in $\mathring{A}$) versus the incident ion energy (in eV) for both the ^{3}He (solid black circles) and the ^{4}He (open circles) implantations. The total length of each error bar is two standard deviations in the mean (Δx_m), i.e., plus or minus one Δx_m. The quantity Δx_m is given by:

$$\Delta x_m = \Delta x/\sqrt{N}, \qquad (2)$$

where N was the total number of helium events detected at a particular incident ion energy for the composite profile. Figure 7 clearly shows that the quantity Δx_m was negligibly small when N exceeded 50 events. The smallest sample size was for the 100 eV ^{4}He implantation where N was equal to 21 events. In this case Δx_m was 3.5 Å and the fractional standard error ($\Delta x_m/\bar{x}$) was $\sim$0.19. This was the only data point that laid slightly below the smooth line that passed through all the other data points for the ^{4}He implantations.

The results presented in fig. 7 show that $\bar{x}$ for both ^{3}He and ^{4}He increased monotonically, although not linearly, with increasing incident helium ion energy. Overall, for both ^{3}He and ^{4}He, the value of $\bar{x}$ increased from 18.7 to 194.9 Å as the incident ion energy was increased from 100 to 1500 eV. For an incident helium ion energy of less than 600 eV the $\bar{x}$'s for ^{3}He were greater than the $\bar{x}$'s for ^{4}He; this indicated that ^{3}He penetrated more deeply into the lattice, on the average, than ^{4}He. This is the result expected for a lighter species implanted in an amorphous solid. At incident helium ion energies greater than 600 eV the $\bar{x}$'s for ^{4}He exceeded the $\bar{x}$'s for ^{3}He. A detailed discussion of these effects is given elsewhere (Amano, Wagner and Seidman[72]).

Figure 8 displays Δx as a function of the incident helium ion energy for both ^{3}He and ^{4}He; Δx is very commonly known as the straggling, since it determines the width of the range profile. The length of each error bar in fig. 8 is equal to two universe standard deviations in the sample standard deviation (Δx_s), i.e., plus or minus one Δx_s. The quantity Δx_s, for a normal distribution, is given by (Parratt[71])

$$\Delta x_s = \Delta x/\sqrt{2N} \quad . \tag{3}$$

We have used eqn. (3) to obtain approximate values of Δx_s for our range profiles which are actually skewed from a normal distribution. It is seen from fig. 8 that for the sample sizes we employed the values of Δx_s were all rather small.

For both ^{3}He and ^{4}He the value of Δx increased monotonically, although not linearly, with increasing incident helium ion energy (see fig. 8). The quantity Δx ranged from 16 to 124 Å as the incident helium ion energy was increased from 100 to 1500 eV. At an incident helium ion energy of $\sim$300 eV the two curves crossed one another and the Δx's for ^{4}He were greater than those for ^{3}He. This indicated that as the incident ion energy was increased the ^{4}He was distributed in space, both wider and deeper than ^{3}He.

Figure 9 exhibits the relative variance $[(\Delta x)^2/(\bar{x})^2]$, of the ^{3}He and ^{4}He range profiles, as a function of the incident helium ion energy (in eV). Within the scatter of the data the quantity $(\Delta x)^2/(\bar{x})^2$ for ^{3}He exhibited a constant value of $\sim$0.47 and the same quantity for ^{4}He was $\sim$0.61. Thus in the energy range 100 to 1500 eV the value of $(\Delta x)^2/(\bar{x})^2$ for ^{4}He was greater than for ^{3}He. This clearly indicated that the ^{4}He was distributed more broadly in space than was ^{3}He.

4.3. Detection of possible radiation damage in the case of the 300 eV helium implantations.

In order to establish that the ^{4}He detected in the case of the 300 eV implantation experiment was not trapped at structural defects in the W lattice, the following isochronal recovery experiment was performed. A W specimen was irradiated along the [110] direction with 300-eV $^4He^+$ ions at $\sim$30 K. After the irradiation $\approx$2(110) planes, corresponding to $\approx$4.48 Å of material, were pulse field evaporated from the specimen. This procedure removed the sputtered surface and restored the surface to a nearly perfect state. The specimen was then warmed isochronally from $\approx$30 to 90 K at a rate of 1.5 K min^{-1}, while the FIM image was photographed at a rate of two 35-mm cine frames sec^{-1}. No SIA contrast effects were observed during this experiment indicating that no SIA's crossed the surface of the FIM specimen. Our previous work[73] demonstrated that if SIA's were present they would have appeared throughout the entire range of 38 to 90 K. The specimen was then dissected by the pulse field-evaporation technique and was examined

for point defects. The density of point defects was determined to be $<8\times10^{-4}$ (atomic fraction); their depth distribution was not related to the ^4He integral profiles. These results constitute conclusive evidence that the ^4He was not trapped at SIA's or vacancies. This indicated that the ^4He atoms were located in the interstices of the lattice and that they were immobile in tungsten at 60.

4.4. The diffusivities of ^3He and ^4He in tungsten.

The temperature at which the interstitial ^4He atoms became mobile in W was determined by implanting ^4He in an FIM specimen at different T_i's and then analyzing at T_r=60 K. The ^4He integral profile determined at T_r was independent of T_i only if the ^4He was immobile at all values of T_i. However, when T_i was above the temperature at which the ^4He interstitials became mobile, the ^4He implanted during the irradiation diffused to the surface of the FIM specimen and entered the gas phase. Therefore a sharp decrease in the measured ^4He concentration was expected as T_i was increased (see fig. 1). Since only T_i was varied, significant changes in the integral profile could only be attributed to a sharp increase in the mobility of the interstitial ^4He atoms at T_i. A dramatic change in the integral profile was observed upon increasing T_i from 90 to 110 K; thus indicating that interstitial ^4He atoms were immobile at 90 K but were highly mobile at 110 K. By employing a diffusion model, a value of the enthalpy change of migration ($\Delta h^m_{^4He}$) of 0.24 to 0.32 eV was estimated. The upper and lower limits on $\Delta h^m_{^4He}$ were determined by the values of the pre-exponential factor (D_o) chosen for the calculation of this quantity; the lower limit was determined by a D_o of $1\times10^{-3}cm^2sec^{-1}$ and the upper limit by a D_o of $1\times10^{-2}cm^2sec^{-1}$.

The diffusivity of ^3He in tungsten was determined by actually following the isothermal recovery of 300 eV implantation profiles which had been implanted at 90, 95, 98, 100 and 110 K. The diffusion equation was solved with appropriate

initial and boundary conditions, to describe the diffusion of ^{3}He out of an FIM tip under isothermal conditions. The fit of the experimental isothermal recovery data to the solution of the diffusion equation yielded the diffusivity of ^{3}He as a function of temperature. The results of this work are shown in fig. 10. It is seen that the data is best described by the expression

$$D(^3\text{He}) = (5.4^{+10.6}_{-3.8})\times 10^{-3} \exp\left[\frac{-0.28\pm0.01\ \text{eV}}{kT}\right] \text{cm}^2\text{sec}^{-1}$$

Thus within the measured experimental uncertainties the Δh's for ^{3}He and ^{4}He in tungsten are identical. For further details on ^{3}He in tungsten see Amano and Seidman.[50]

ACKNOWLEDGEMENTS

This work was supported by the U.S. Department of Energy. Additional support was received from the National Science Foundation through the use of the technical facilities of the Materials Science Center at Cornell University. I wish to thank my co-workers Drs. J. Amano and A. Wagner for permission ot present results (see §4) in advance of more formal publication.

REFERENCES

1. E.W. Müller, Z. Physik 131, 136 (1951).
2. E.W. Müller, J.A. Panitz and S.B. McLane, Rev. Sci. Instrum. 39, 83 (1968).
3. P.J. Turner, P. Cartwright, M.J. Southon, A. van Oostrom and B.W. Manley, J. Sci. Instrum. 2, 731 (1969).
4. S.S. Brenner and J.T. McKinney, Surface Sci. 23, 88 (1970).
5. E.W. Müller and T.T. Tsong, Field-Ion Microscopy (American Elsevier, New York, 1969), Chapt. II.
6. E.W. Müller and T.T. Tsong, Field-Ion Microscopy (American Elsevier, New York, 1969), Chapt. III.
7. R.M. Scanlan, D.L. Styris, D.N. Seidman and D.G. Ast, Cornell Materials Science Center Report No. 1159 (1969).
8. W.P. Poschenrieder, Int. J. Mass Spectrom. and Ion Phys. 9, 357 (1972).
9. E.W. Müller and S.V. Krishnaswamy, Rev. Sci. Instrum. 45, 1053 (1974).
10. R. Gomer, Field Emission and Field-Ionization (Harvard University Press, Cambridge, Massachusetts, 1961).
11. Field-Ion Microscopy, edited by J.J. Hren and S. Ranganathan (Plenum Press, New York, 1968).
12. Applications of Field-Ion Microscopy, edited by R.F. Hochman, E.W. Müller and B. Ralph (Advanced Research Projects Agency, ARDA order No. 878 and the Georgia Institute of Technology, 1969).
13. K.M. Bowkett and D.A. Smith, Field-Ion Microscopy (American Elsevier, New York, 1970).
14. Field-Ion, Field Emission Microscopy and Related Topics, special issue of Surface Science 23, 1 (1970).
15. E.W. Müller and T.T. Tsong, in Progress in Surface Science, edited by S.G. Davison (Pergamon Press, Oxford, 1973), Vol. 4, Part I, pp. 1-139.

16. J.A. Panitz, in Progress in Surface Science, edited by S.G. Davison (Pergamon Press, Oxford, 1978), Vol. 8, pp. 219-62.

17. Proceedings of the Int. Symp. on Application of FIM to Metallurgy, edited by R.R. Hasiguti, Y. Yashiro and N. Igata (Dept. of Metallurgy and Materials Science, Univ. of Tokyo, Tokyo, Japan, 1977).

18. D.N. Seidman, J. Phys. F: Metal Phys. 3, 393 (1973).

19. D.N. Seidman, K.L. Wilson and C.H. Nielsen, in Proceedings of the Int. Conf. on Fundamental Aspects of Radiation Damage in Metals, edited by M.T. Robinson and F.W. Young, Jr. (National Technical Information Service, U.S. Dept. of Commerce, Springfield, Virginia, 1975), pp. 373-96.

20. D.N. Seidman, in Radiation Damage in Metals, edited by N.L. Peterson and S.D. Harkness (American Society for Metals, Metals Park, Ohio, 1976), pp. 28-57.

21. D.N. Seidman, Surface Sci. 70, 532 (1978).

22. A. Wagner, T.M. Hall and D.N. Seidman, Rev. Sci. Instrum. 46, 1032 (1975).

23. T.M. Hall, A. Wagner, A.S. Berger and D.N. Seidman, Cornell Materials Science Center Report No. 2357 (1975).

24. T.M. Hall, A. Wagner, A.S. Berger and D.N. Seidman, Scripta Met. 10, 485 (1976).

25. T.M. Hall, A. Wagner and D.N. Seidman, J. Phys. E: Sci. Instrum. 10, 884 (1977).

26. A. Wagner, T.M. Hall and D.N. Seidman, J. Nuc. Mat. 69 & 70, 532 (1978).

27. R.M. Scanlan, D.L. Styris and D.N. Seidman, Phil. Mag. 23, 1439 (1971).

28. R.M. Scanlan, D.L. Styris and D.N. Seidman, Phil. Mag. 23, 1459 (1971).

29. P. Pétroff and D.N. Seidman, Appl. Phys. Lett. 18, 518 (1971).

30. D.N. Seidman and K.H. Lie, Acta Met. 20, 1045 (1972).

31. P. Pétroff and D.N. Seidman, Acta Met. 21, 323 (1973).

32. J.T. Robertson, K.L. Wilson and D.N. Seidman, Phil. Mag. 27, 1417 (1973).

33. D.N. Seidman, K.L. Wilson and C.H. Nielsen, Phys. Rev. Lett. 35, 1041 (1975).

34. K.L. Wilson and D.N. Seidman, Rad. Effects 33, 149 (1977).

35. D.N. Seidman, Scripta Met. 13, 251 (1979).

36. K.L. Wilson, M.I. Baskes and D.N. Seidman, Cornell Materials Science Center Report #4055 (1979); submitted to Acta Metallurgica for publication.

37. C.H. Nielsen, M.S. Thesis, Cornell University (1977).

38. J. Aidelberg, Ph.D. Thesis (in preparation), Cornell University (1979).

39. C-Y. Wei and D.N. Seidman, Rad. Effects 32, 229 (1977).

40. C-Y. Wei and D.N. Seidman, J. Nuc. Mat. 69&70, 693 (1978).

41. K.L. Wilson and D.N. Seidman, Rad. Effects 27, 67 (1975).

42. A.S. Berger, D.N. Seidman and R. W. Balluffi, Acta Met. 21, 123 (1973).

43. A.S. Berger, D.N. Seidman and R.W. Balluffi, Acta Met. 21, 323 (1973).

44. J.Y. Park, H-C. W. Huang, A.S. Berger, and R.W. Balluffi, in Defects and Defect Clusters in B.C.C. Metals and Their Alloys, edited by R.J. Arsenault (University of Maryland, College Park, MD, 1973), Nuclear Metallurgy, Vol. 18, pp. 420-439.

45. J.Y. Park, Ph.D. Thesis, Cornell University (1975).

46. H-C. W. Huang, Ph.D. Thesis, Cornell University (1975).

47. A. Wagner and D.N. Seidman, Phys. Rev. Letts. 42, 515 (1979).

48. A. Wagner, Ph.D. Thesis, Cornell University (1978).

49. D.N. Seidman, Department of Energy Report #C00-3158-77 (1979).

50. J. Amano and D.N. Seidman, to be published. (1979).

51. A. Macrander and D.N. Seidman, unpublished work (1979).

52. M. Yamamoto and D.N. Seidman, work in progress (1979).

53. L.A. Beavan, R.M. Scanlan and D.N. Seidman, Acta Metallurgica 19, 1339 (1971).

54. K.L. Wilson and D.N. Seidman, in Defects and Defect Clusters in B.C.C. Metals and Their Alloys, edited by R.J. Arsenault (University of Maryland, College Park, MD, 1973), Nuclear Metallurgy, Vol. 18, pp. 420-439.

55. C.-Y. Wei and D.N. Seidman, Phil. Mag. A, 37, 257 (1978).

56. C.-Y. Wei, Ph.D. Thesis, Cornell University (1978).

57. M.I. Current and D.N. Seidman, to be published (1979).

58. S.S. Brenner and D.N. Seidman, Rad. Effects 24, 73 (1975).

59. S.S. Brenner, R. Wagner, J. Spitznagel, Met. Trans. A, 9A, 1761 (1978).

60. A. Wagner and D.N. Seidman, Cornell Materials Science Center Report #4007 (1978); to appear in J. Nuc. Mat. (1979).

61. C.-Y. Wei and D.N. Seidman, Cornell Materials Science Center, Report #4088 (1979).

62. Radiation-Induced Voids in Metals, edited by J.W. Corbett and L.C. Ianniello (National Technical Information Service, Springfield, Va., 1972).

63. See, for example, J.Nuc. Mater. 53 (1974), 76 (1978), and 77 (1978).

64. W.D. Wilson and C.L. Bisson, Radiat. Effects 22, 63 (1974).

65. O.S. Oen and M.T. Robinson, Nuc. Instrum. Methods 132, 647 (1976).

66. D.J. Reed, Radiat. Effects 31, 129 (1977).

67. B. Terreault, R.G. St-Jacques, G. Veilleaux, J.G. Martel, J. L'Ecuger, C. Brassard, and C. Cardinal, Can. J. Phys. 56, 235 (1978).

68. E.V. Kornelsen, Radiat. Effects 13, 227 (1972).

69. F. Maury, M. Biget, P. Vajda, A. Lucasson, P. Lucusson, Radiat. Effects 38, 53 (1978).

70. J.P. Biersack and L.D. Haggmark, submitted to Nuc. Instrum. Methods (1979).

71. L.G. Parratt, Probability and Experimental Errors in Science (John Wiley, New York, 1961), Chapt. 2.

72. J. Amano, A. Wagner and D.N. Seidman, Cornell Materials Science Center Report #4108 (1979).

73. R.M. Scanlan, D.L. Styris, and D.N. Seidman, Philos. Mag. 23, 1439 (1971); K.L. Wilson and D.N. Seidman, Radiation Effects 27, 67 (1975); D.N. Seidman, K.L. Wilson, and C.H. Nielsen, Phys. Rev. Lett. 35, 1041 (1975).

FIGURE CAPTIONS

Fig. 1. (a) The in situ irradiation of a W FIM specimen with 300-eV $^4He^+$ ions at a T_i where the implanted ^4He atoms are immobile. The density of spots corresponds to the approximate range profile of ^4He in W. The cylindrical volume element represents the volume chemically analyzed by the atom probe. (b) The number of ^4He atoms versus depth as a function of T_i. Note that the ^4He integral profile tends to flatten out as a T_i is increased. (c) The range profiles of ^4He in W as a function of T_i.

Fig. 2. A schematic diagram illustrating the method employed to determine an absolute depth scale. Three states in the field evaporation of one (110) plane of W are shown in (a). The field-evaporation behavior of this plane is indicated in (b) by the steplike increase in the rate at which tungsten atoms are detected.

Fig. 3. The ^3He integral profiles for the implantation energies of 100, 500 and 1500 eV. The tungsten specimens were implanted to 60 K parallel to the [110] direction.

Fig. 4. A composite ^3He range profile for all the 300 eV implantations at 60 K. A total of 385 ^3He events were involved in the construction of this range profile.

Fig. 5. The ^4He integral profiles for the implantation energies of 150, (475 and 500), and 1000 eV. The tungsten specimens were implanted at 60 K parallel to the [110] direction.

Fig. 6. A composite ^4He range profile for all the 1000 eV implantations at 60 K. A total of 147 ^4He events were recorded in the construction of this range profile.

Fig. 7. The mean range ($\bar{x}$) in angstroms versus the incident helium energy (eV) for all the ^{3}He and ^{4}He implantations in tungsten at 60 K.

Fig. 8. The standard deviation or straggling in angstroms (Δx) versus the incident helium energy (eV) for all the ^{3}He and ^{4}He implantations in tungsten at 60 K.

Fig. 9. The relative variance $[(\Delta x)^2/(\bar{x})^2]$ versus the incident helium energy (eV) for all the ^{3}He and ^{4}He implantations in tungsten at 60 K.

Fig. 10. The diffusion coefficient of ^{3}He versus (1/T) in the temperature range 90 to 110 K. The times indicated correspond to different recovery times at each temperature.

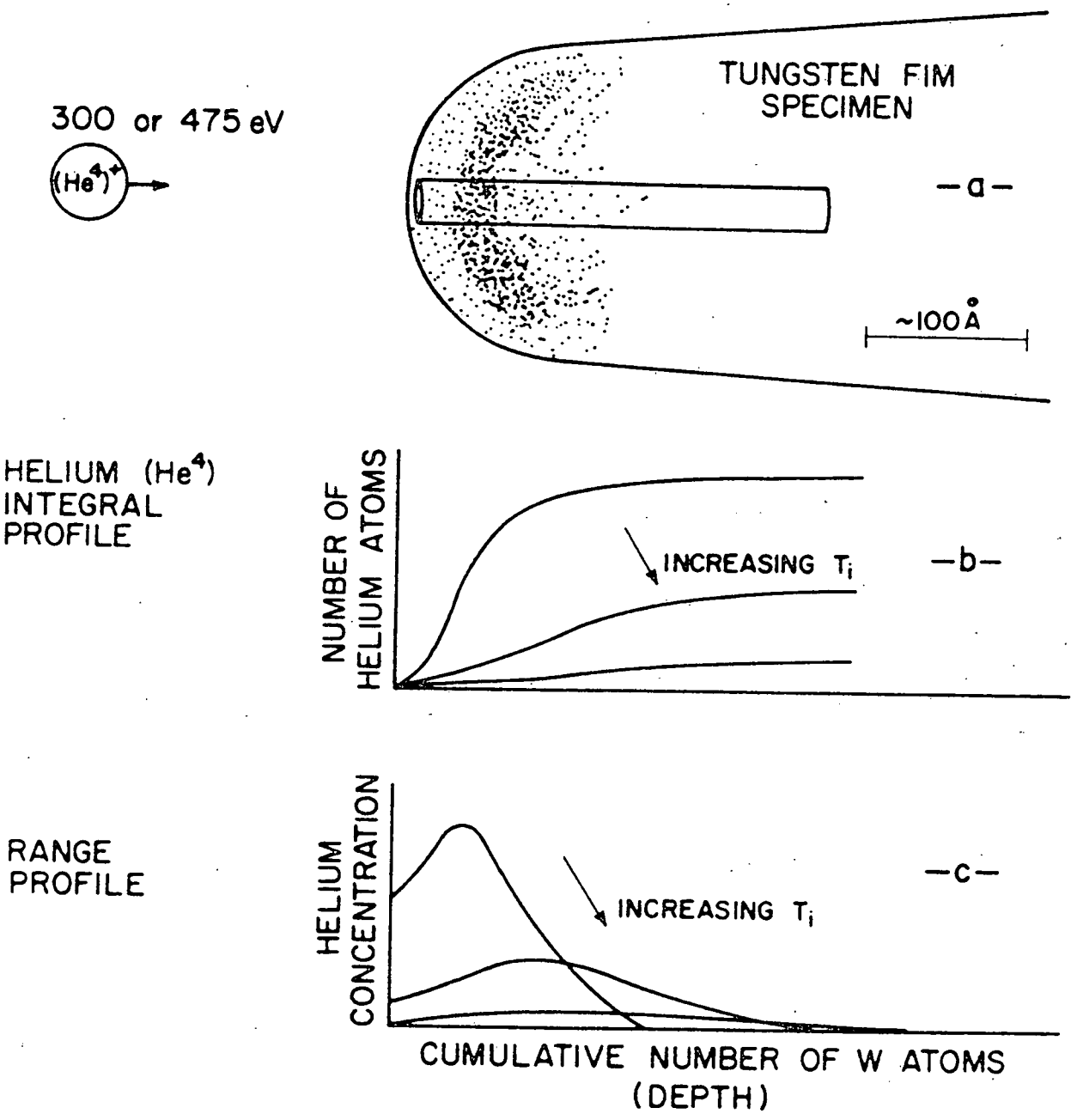
300 or 475 eV
$(He^4)^+$
TUNGSTEN FIM SPECIMEN
—a—
~100 Å
HELIUM (He^4) INTEGRAL PROFILE
NUMBER OF HELIUM ATOMS
INCREASING T_i
—b—
RANGE PROFILE
HELIUM CONCENTRATION
INCREASING T_i
—c—
CUMULATIVE NUMBER OF W ATOMS (DEPTH)

Fig. 1

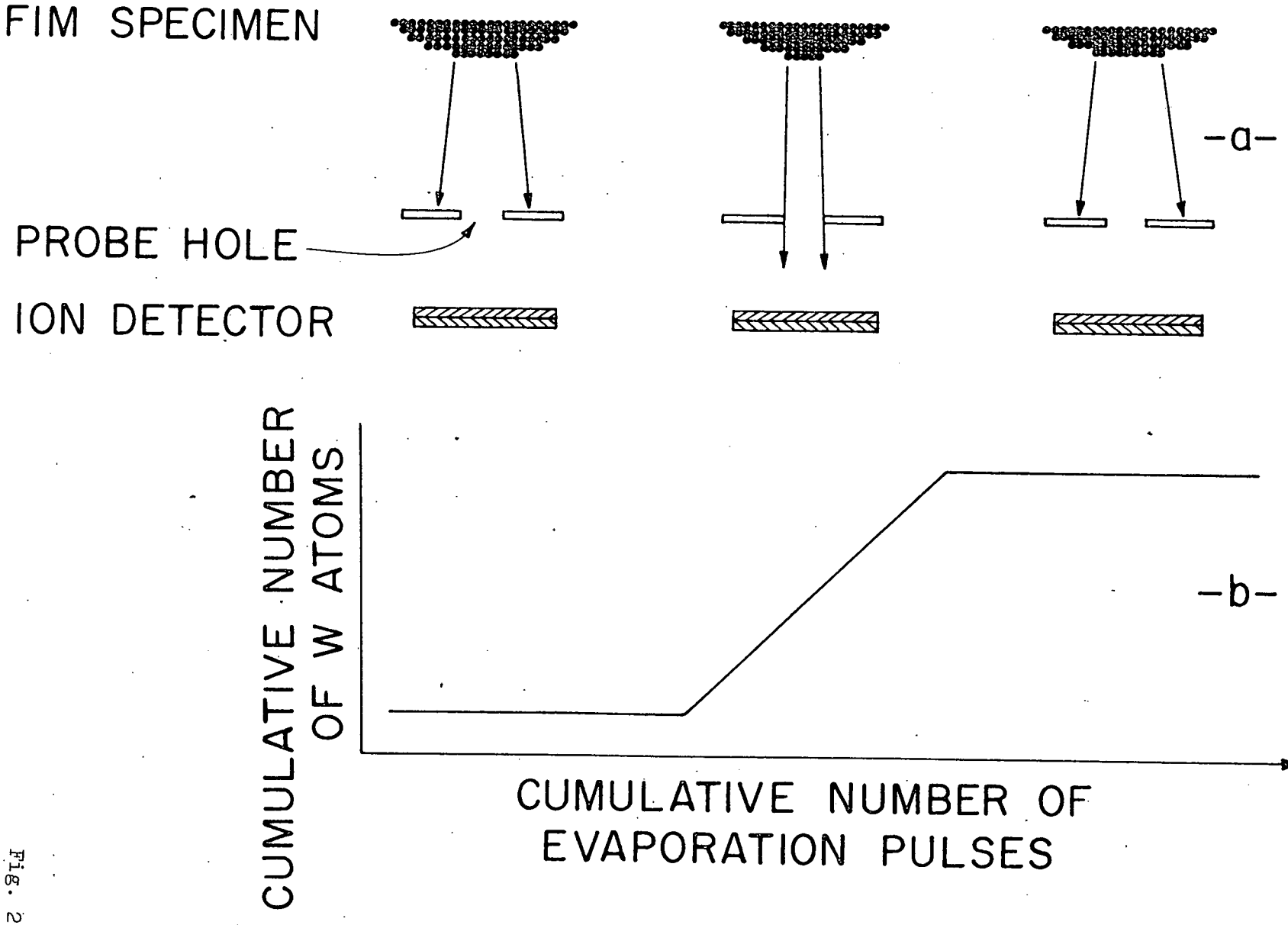
FIM SPECIMEN
PROBE HOLE
ION DETECTOR
-a-
-b-
CUMULATIVE NUMBER OF W ATOMS
CUMULATIVE NUMBER OF EVAPORATION PULSES

Fig. 2

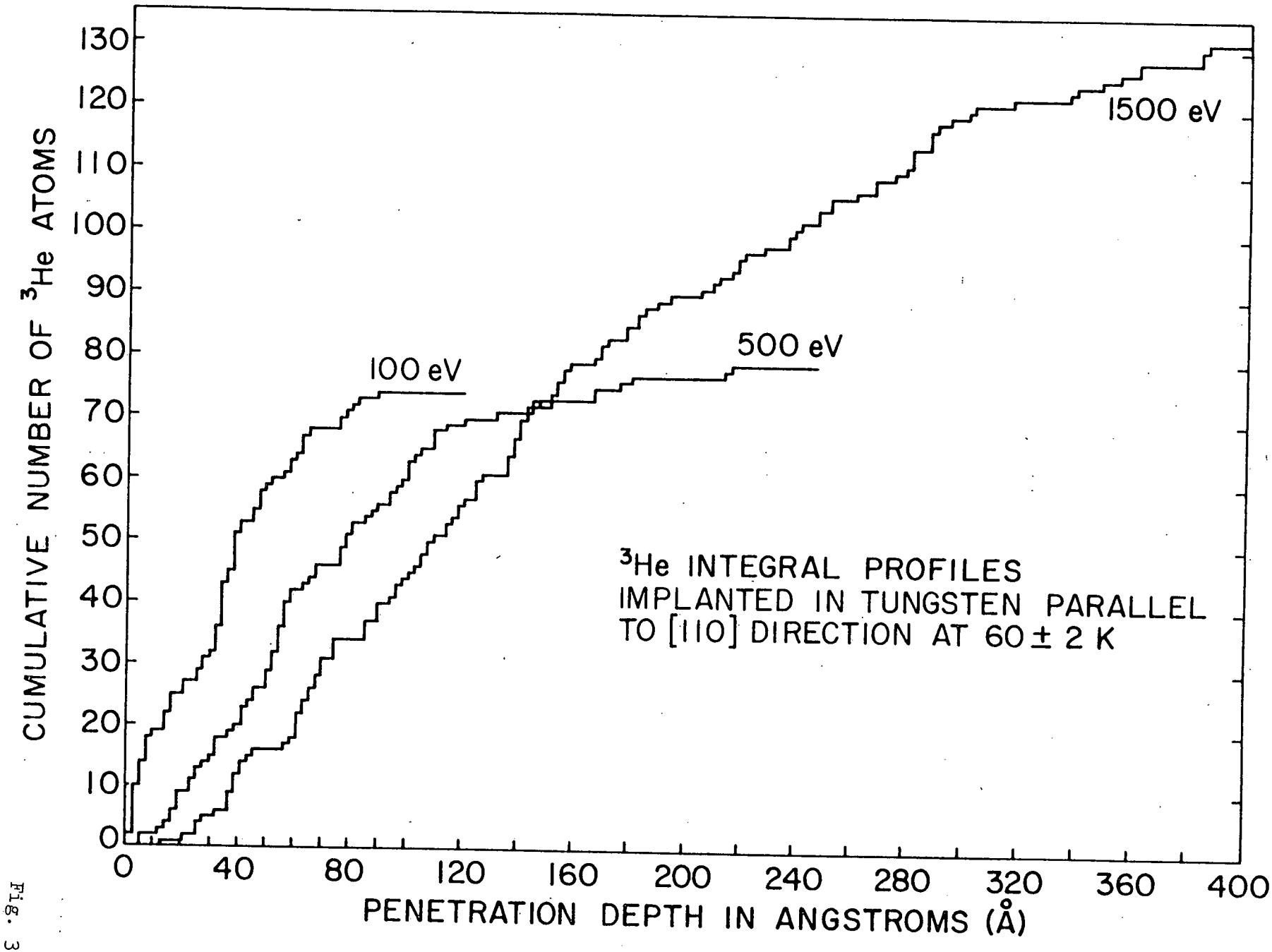
CUMULATIVE NUMBER OF ^{3}He ATOMS
PENETRATION DEPTH IN ANGSTROMS (Å)
100 eV
500 eV
1500 eV
^{3}He INTEGRAL PROFILES
IMPLANTED IN TUNGSTEN PARALLEL
TO [110] DIRECTION AT 60 ± 2 K
0
10
20
30
40
50
60
70
80
90
100
110
120
130
0
40
80
120
160
200
240
280
320
360
400

Fig. 3

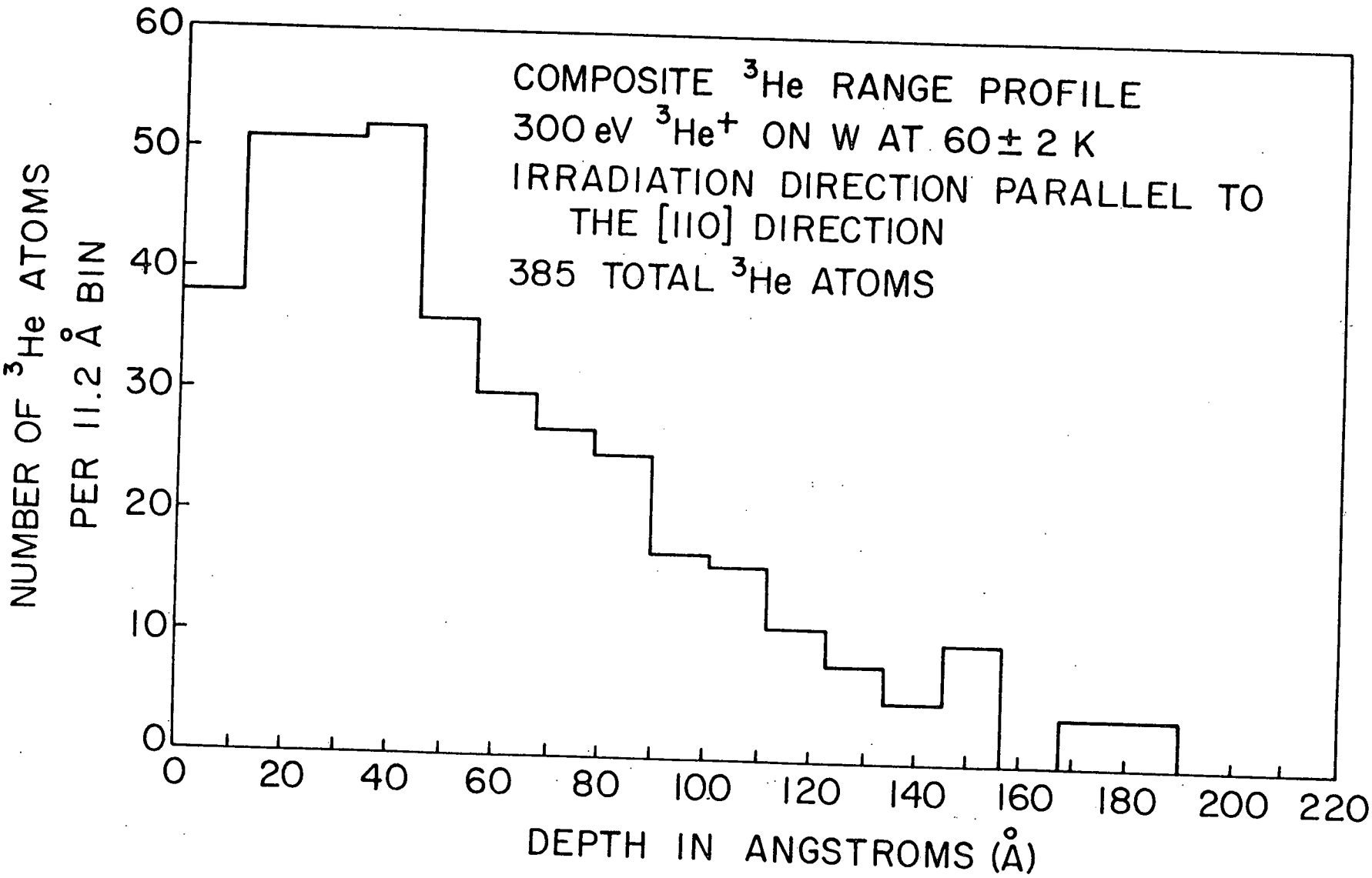
COMPOSITE ^{3}He RANGE PROFILE
300 eV ^{3}He$^+$ ON W AT 60 ± 2 K
IRRADIATION DIRECTION PARALLEL TO THE [110] DIRECTION
385 TOTAL ^{3}He ATOMS
NUMBER OF ^{3}He ATOMS PER 11.2 Å BIN
DEPTH IN ANGSTROMS (Å)
0
10
20
30
40
50
60
0
20
40
60
80
100
120
140
160
180
200
220

Fig. 4

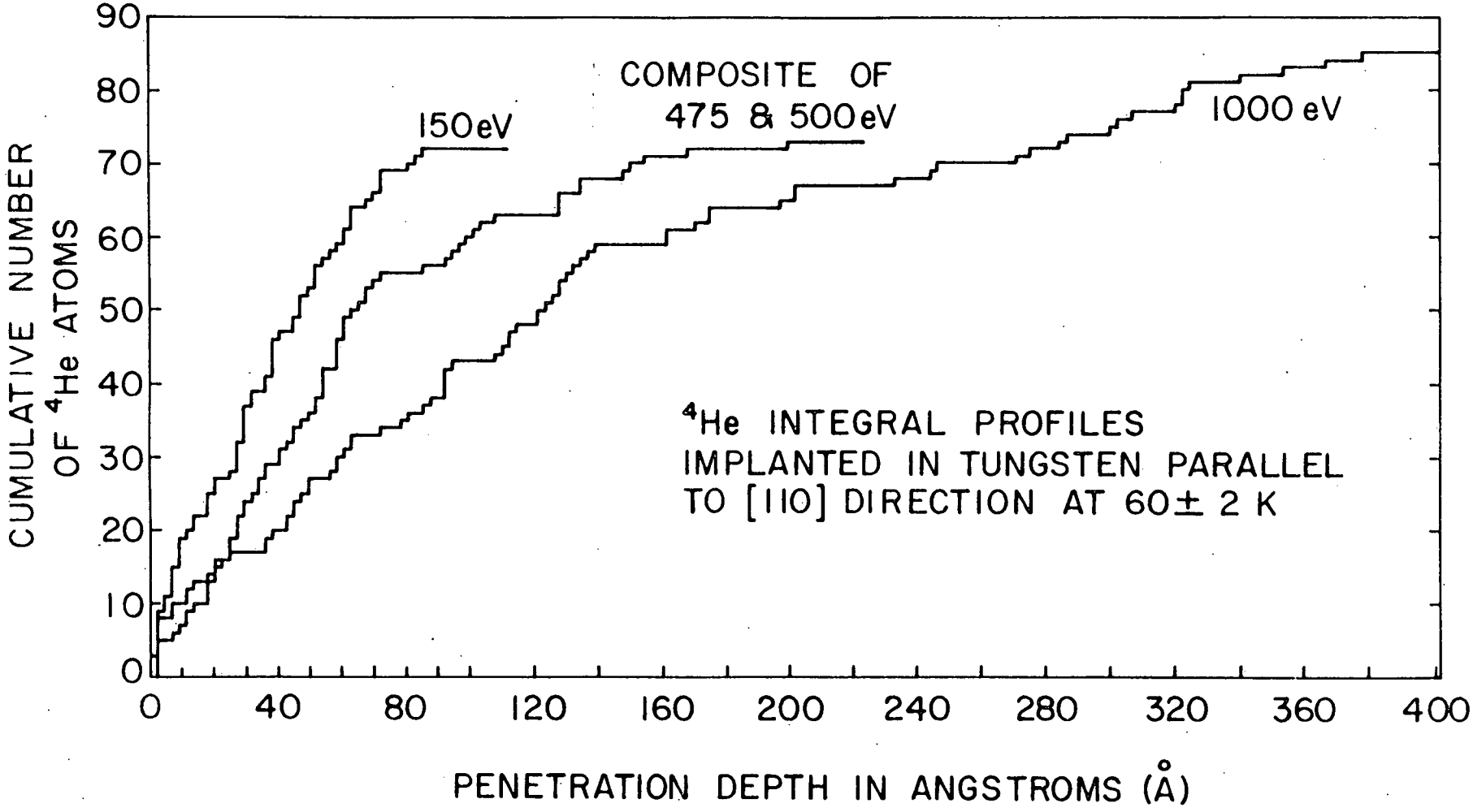
CUMULATIVE NUMBER OF ^{4}He ATOMS
90
80
70
60
50
40
30
20
10
0
150eV
COMPOSITE OF 475 & 500eV
1000 eV
^{4}He INTEGRAL PROFILES IMPLANTED IN TUNGSTEN PARALLEL TO [110] DIRECTION AT 60± 2 K
0
40
80
120
160
200
240
280
320
360
400
PENETRATION DEPTH IN ANGSTROMS (Å)

Fig. 5

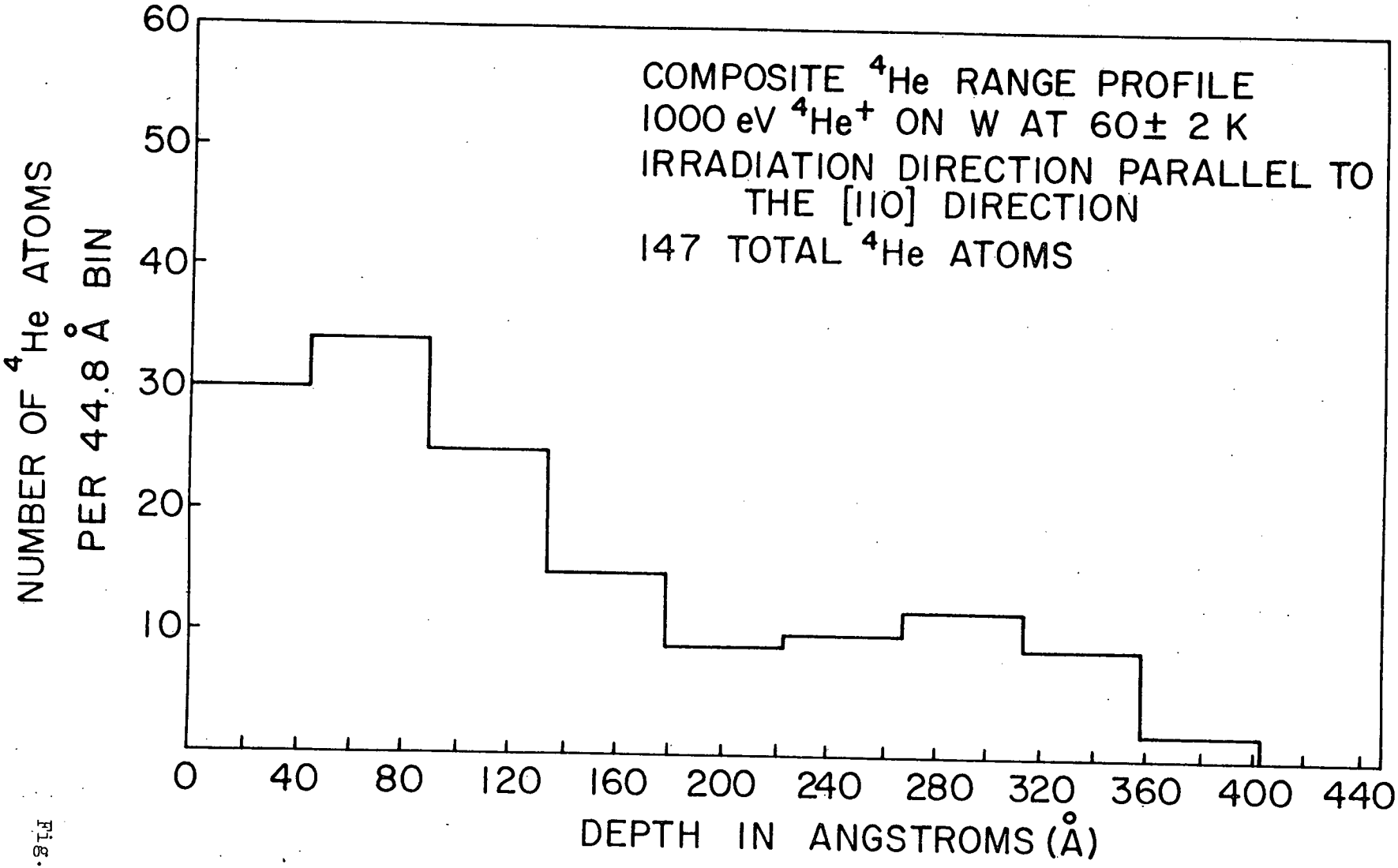
COMPOSITE ^{4}He RANGE PROFILE
1000 eV ^{4}He$^+$ ON W AT 60± 2 K
IRRADIATION DIRECTION PARALLEL TO THE [110] DIRECTION
147 TOTAL ^{4}He ATOMS
NUMBER OF ^{4}He ATOMS PER 44.8 Å BIN
60
50
40
30
20
10
0
40
80
120
160
200
240
280
320
360
400
440
DEPTH IN ANGSTROMS (Å)

FIG. 6

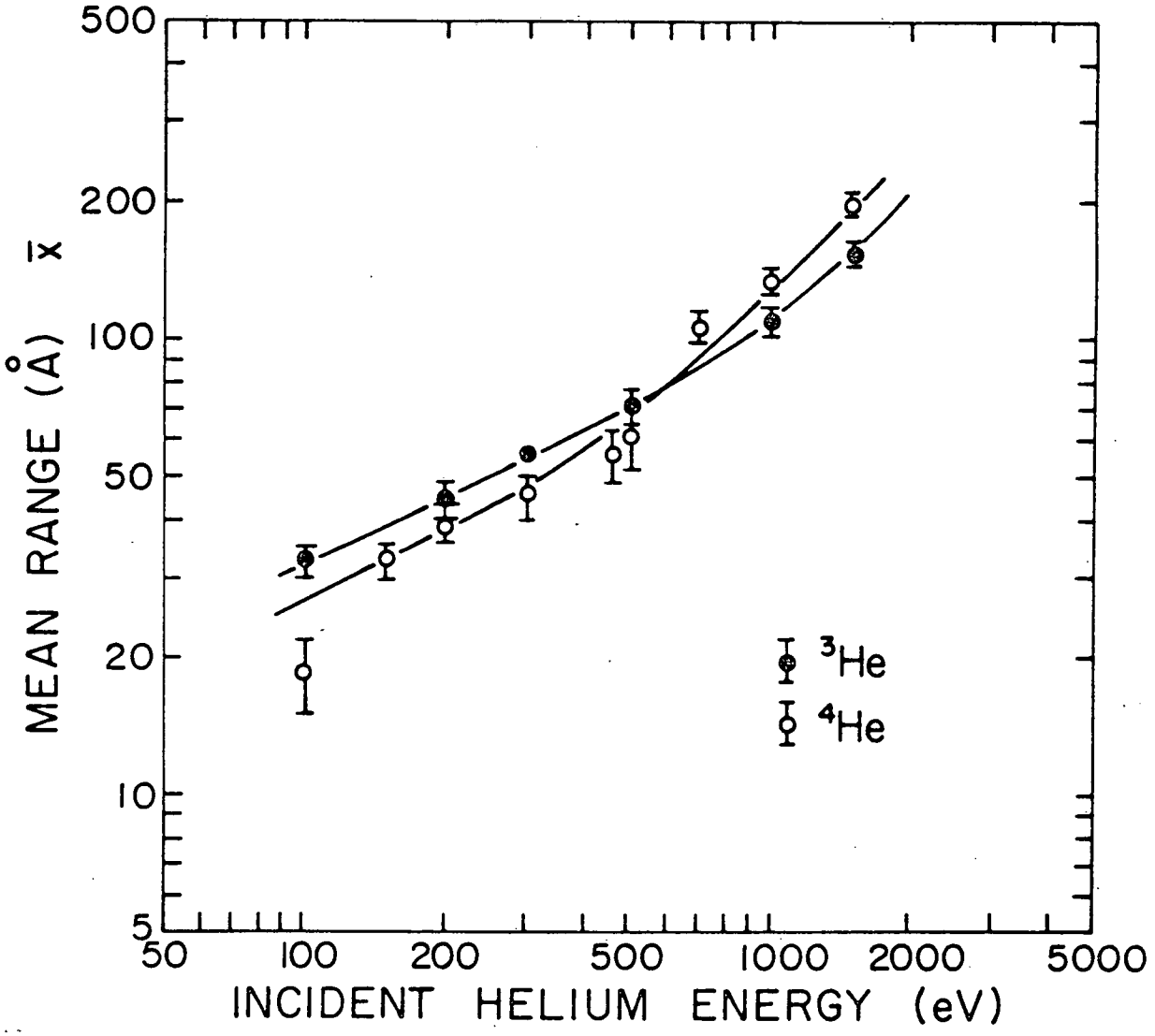
500
200
100
50
20
10
5
MEAN RANGE (Å) $\bar{x}$
50
100
200
500
1000
2000
5000
INCIDENT HELIUM ENERGY (eV)
^{3}He
^{4}He

Fig. 7

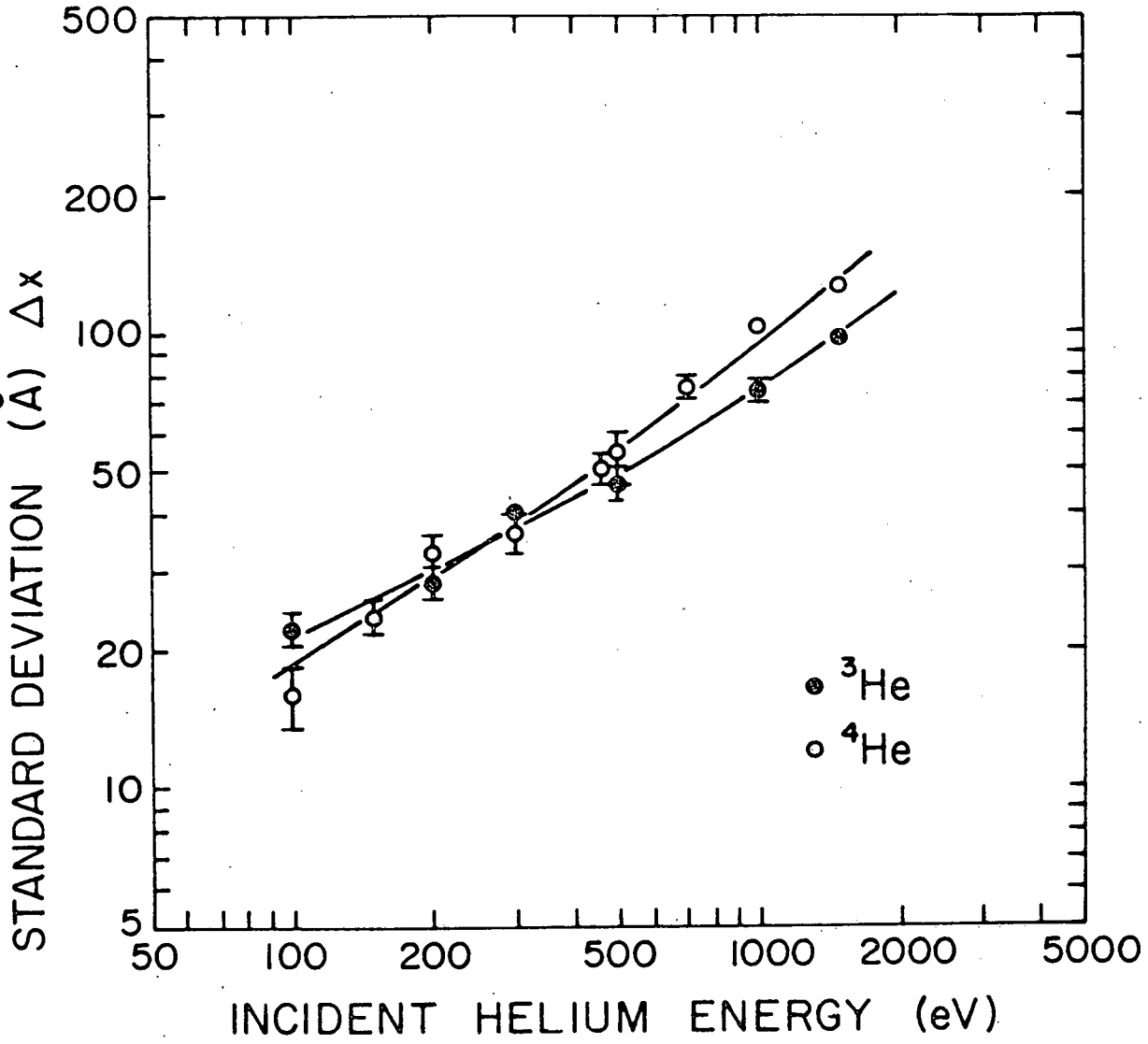
500
200
100
50
20
10
5
STANDARD DEVIATION (Å) Δx
50
100
200
500
1000
2000
5000
INCIDENT HELIUM ENERGY (eV)
³He
⁴He

Fig. 8

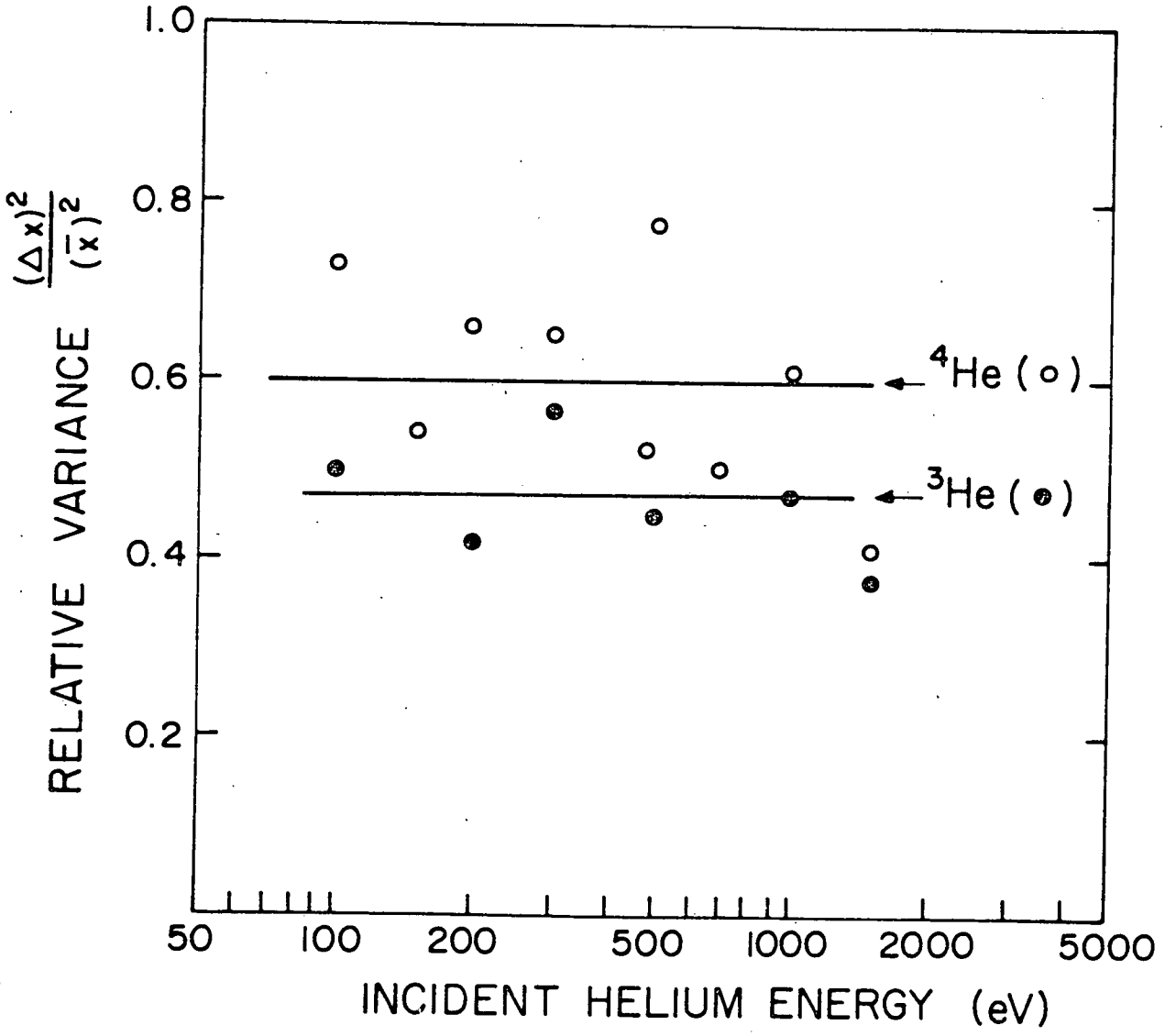
1.0
0.8
0.6
0.4
0.2
$\frac{(\Delta x)^2}{(\bar{x})^2}$
RELATIVE VARIANCE
^{4}He (o)
^{3}He (●)
50
100
200
500
1000
2000
5000
INCIDENT HELIUM ENERGY (eV)

Fig. 9

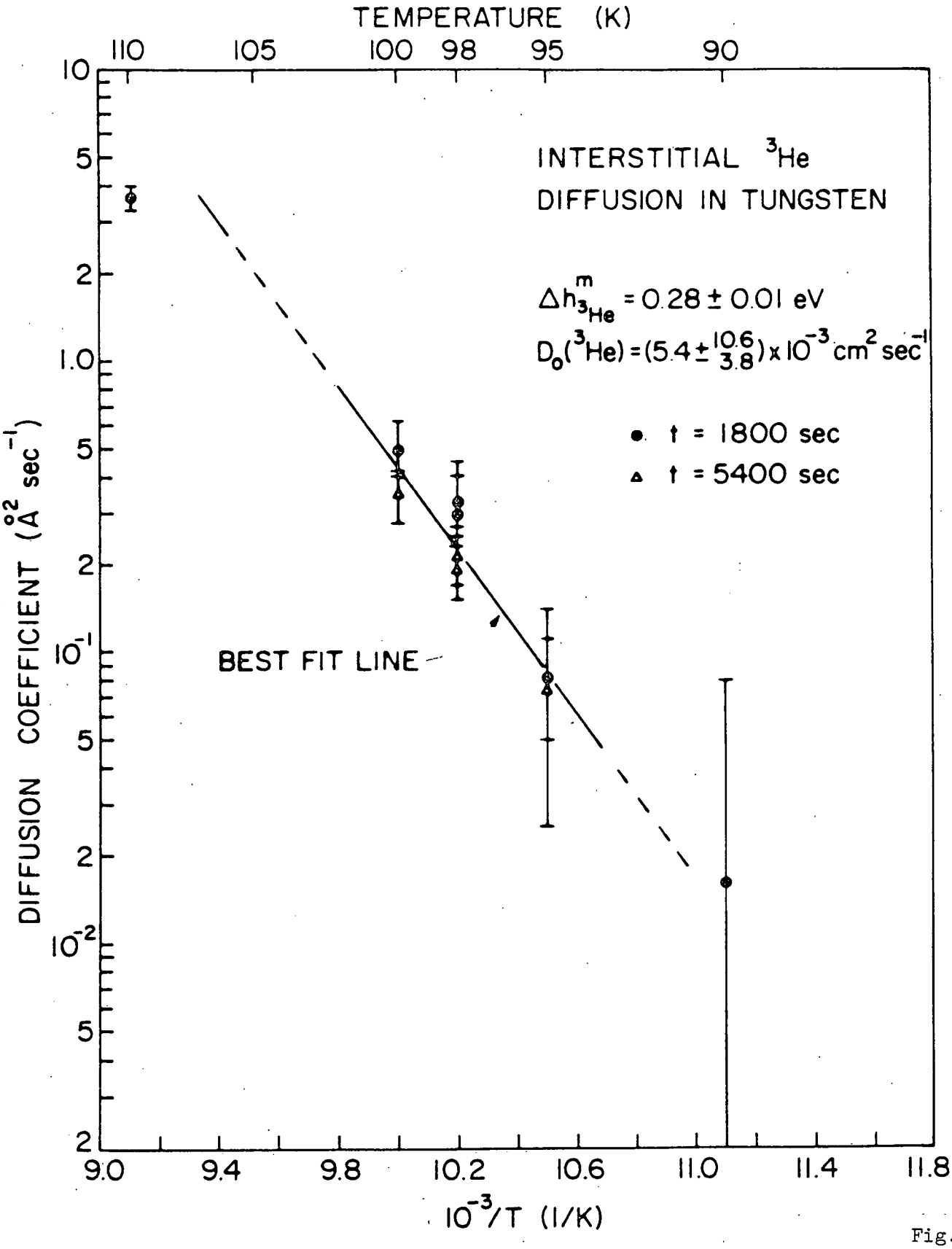
TEMPERATURE (K)
110
105
100
98
95
90
INTERSTITIAL ^{3}He
DIFFUSION IN TUNGSTEN
$\Delta h^m_{^3He} = 0.28 \pm 0.01$ eV
$D_o(^3He) = (5.4 \pm \frac{10.6}{3.8}) \times 10^{-3}$ cm^2 sec^{-1}
● t = 1800 sec
△ t = 5400 sec
BEST FIT LINE
DIFFUSION COEFFICIENT (Å^2 sec^{-1})
10
5
2
1.0
5
2
10^{-1}
5
2
10^{-2}
5
2
9.0
9.4
9.8
10.2
10.6
11.0
11.4
11.8
10^{-3}/T (1/K)

Fig. 10